



Microanalytical methods for in-situ high-resolution analysis of rock varnish at the micrometer to nanometer scale



D.S. Macholdt^{a,*}, K.P. Jochum^a, C. Pöhlker^a, B. Stoll^a, U. Weis^a, B. Weber^b, M. Müller^c, M. Kappl^c, S. Buhre^d, A.L.D. Kilcoyne^e, M. Weigand^f, D. Scholz^d, A.M. Al-Amri^g, M.O. Andreae^{a,g}

^a Biogeochemistry Department, Max Planck Institute for Chemistry, Mainz, Germany

^b Multiphase Chemistry Department, Max Planck Institute for Chemistry, Mainz, Germany

^c Physics of Interfaces Department, Max Planck Institute for Polymer Research, Mainz, Germany

^d Institute of Geosciences, Johannes Gutenberg University, Mainz, Germany

^e Lawrence Berkeley National Laboratory, Berkeley, CA, United States

^f Modern Magnetic Systems Department, Max Planck Institute for Intelligent Systems, Stuttgart, Germany

^g Geology and Geophysics Department, King Saud University, Riyadh, Saudi Arabia

ARTICLE INFO

Article history:

Received 9 December 2014

Received in revised form 22 May 2015

Accepted 23 June 2015

Available online 30 June 2015

Keywords:

Rock varnish

Desert varnish

Femtosecond LA-ICP-MS

EPMA

STXM-NEXAFS

FIB slicing

ABSTRACT

A wide range of analytical techniques were used to investigate rock varnish from different locations (Negev, Israel; Knersvlakte, South Africa; Death Valley and Mojave Desert, California): a 200 nm-femtosecond laser ablation-inductively coupled plasma-mass spectrometer (LA-ICP-MS), an electron probe microanalyzer (EPMA), focused ion beam (FIB) slicing, and scanning transmission X-ray microscopy–near edge X-ray absorption fine structure spectroscopy (STXM–NEXAFS). This combination enables comprehensive high-spatial-resolution analysis of rock varnish. Femtosecond LA-ICP-MS and EPMA were used for quantitative determination of element concentrations. In-situ measurements were conducted on thick and thin sections with a resolution of 10–40 μm and 2 μm , respectively. The results demonstrate that some elements, such as Mn, Co, Pb, Ni, and Cu, are highly enriched in varnish relative to the upper continental crust (up to a factor of 100). The varnish composition is not influenced by the composition of the underlying rock, which is witnessed by plots of MnO₂ vs. SiO₂ contents. Furthermore, the Mn-free end members fall in the range of average dust compositions.

The varnishes from the various locations show distinct differences in some elemental ratios, in particular Mn/Fe (0.3–25.1), Mn/Ba (4–170), Ni/Co (0.03–1.8) and Pb/Ni (0.4–23). The rare earth element (REE) patterns vary with La_N/Yb_N = 3.5–12 and different degrees of Ce anomalies (Ce/Ce* = 1.5–5.3).

To study the internal structure of the varnish, 100–200 nm thick FIB slices were prepared and mappings of Fe, Mn, N, CO₂²⁻, Ca, C, and Si at the nm scale performed. Banded internal structures of Mn, Fe and organic C were observed in the Israeli and Californian samples, however, no Fe-rich layers are present in the South African rock varnish samples. Furthermore, cavities were found that are partly filled by C, Fe, and Mn rich material. Internal structures are different for varnish from different locations, which might reflect different types of genesis. The results of the combined microanalytical techniques give important detailed insights towards unraveling the genesis of rock varnish.

© 2015 Elsevier B.V. All rights reserved.

1. Introduction

The genesis of rock varnish has been a matter of debate since 1812, when Alexander von Humboldt first observed it at the cataracts of the Orinoco River (Von Humboldt and Bonpland, 1819, Dorn et al., 2012a). Meanwhile, similar rock varnishes have been observed in a wide variety of terrestrial environments and there have been quite a number of studies discussing the origin of these coatings. Both biological and inorganic processes, as well as a combination of both, have been suggested.

Rock varnish is a black, sometimes red or brown, shiny layer on rock surfaces, present on slowly weathering rocks, independent of their lithology (Engel and Sharp, 1958). The main components of varnish are poorly crystallized Mn oxides (usually hollandite–todorokite, birnessite and buserite, poorly crystallized phyllo-manganates of unspecified types, and Mn–Fe spinel), poorly crystallized Fe oxides (e.g., hematite, Fe₂O₃), and clay minerals (Potter and Rossman, 1979; Garvie et al., 2008). The clay mineral fraction in varnish, reaching up to 70% of the varnish volume (Thiagarajan and Lee, 2004) is most likely introduced by the atmospheric deposition of dust (Thiagarajan and Lee, 2004), whereas the origin and precipitation of Mn are not yet fully understood.

Manganese has an abundance of 0.1% (as Mn oxide, MnO) in the upper continental crust, while it is enriched up to 40% (as MnO₂) in

* Corresponding author at: P.O. Box 3060, 55020 Mainz, Germany.
E-mail address: d.macholdt@mpic.de (D.S. Macholdt).

rock varnish (Rudnick and Gao, 2003). Therefore, it has to be preferentially reduced and dissolved from dust, and re-precipitated by oxidation for the formation of varnish. One suggestion is a chemical reduction and precipitation under the pH (5.7) and Eh (~0.8) conditions of rainwater (Thiagarajan and Lee, 2004). The second hypothesis is biological reduction by Mn reducing bacteria (Perry and Kolb, 2004). SiO₂ is also found in large amounts in varnish, as a component of the clay mineral fraction and as silica glaze, and has been suggested to be involved in varnish formation (Perry et al., 2006; Wang et al., 2011). Varnish grows in almost every type of terrestrial weathering environment (Krinsley et al., 2009; Krinsley et al., 2012), but distinctive varnishes are found in arid to semi-arid desert climates. Desert varnish is of specific interest, since it has been suggested as a possible paleoclimate archive (Perry and Adams, 1978; Liu and Dorn, 1996). Since there are almost no climate archives present in deserts, especially beyond the range of ¹⁴C dating, rock varnish might be an important tool in bridging this gap (Broecker and Liu, 2001). An understanding of its genesis is therefore required.

Estimates of the growth rate of rock varnish vary between 1 and 640 μm per 1000 a (Liu and Broecker, 2000; Spilde et al., 2013), with its maximum thickness rarely exceeding about 250 μm (Northup et al., 2010). The growth rates seem to depend on the humidity of the environment, with slower growth rates for desert climates (Krinsley et al., 2012).

Many studies on varnish and its composition have been published (Reneau et al., 1992; Thiagarajan and Lee, 2004; Dorn, 2008; Goldsmith et al., 2014) with differing techniques. Detailed information on used techniques are provided by Krinsley et al. (2013). However, only a few studies examined the major element distribution in combination with trace element measurements at the μm to nm scale.

Since varnish is a micrometer-scale, thin crust, the aim of this paper is to combine different microanalytical techniques to investigate samples from different locations, USA, Israel and South Africa, at μm to nm scales. Each technique provides additional and complementary information for understanding the structures within rock varnish:

- a femtosecond laser ablation-inductively coupled plasma-mass spectrometer (fs LA-ICP-MS) with a spatial resolution of 10–40 μm provides precise and accurate determination of major, and in particular, trace element concentrations,
- an electron probe microanalyzer (EPMA) yields major element measurements at a scale of a few micrometers,

- scanning transmission X-ray microscopy–near edge X-ray adsorption fine structure spectroscopy (STXM–NEXAFS), using focused ion beam (FIB) milled ultra-thin sections, contributes element distribution mappings at the nanometer scale.

2. Analytical methods

2.1. Samples

Rock samples covered with varnish were collected at different sampling sites in the Mojave Desert (California, USA, Fig. 1a), the Negev Desert (Israel, Fig. 1b), and the Knersvlakte (South Africa, Fig. 1c) during several field campaigns from 2010 to 2014. The Mojave and Negev deserts have arid climates, while the Knersvlakte is a semi-arid desert. Varnish samples were chosen in the field, giving preference to darker coatings which would therefore presumably have a thicker varnish crust. All rocks from California and South Africa were taken from the ground, and therefore consist of pebbles and small rocks (a few to tens of centimeters) which had direct contact to the underlying soil. The Israeli samples were collected as fragments or chips from larger boulders (Table 1) and were subdivided into those with a macroscopical botryoidal surface structure, and those with a smooth and flat surface. The South African samples, mostly pebbles of a few cm, had a black, shiny varnish crust with metallic luster on their tops and a slightly duller tinge on the bottom sides. The top and bottom sides of the rocks were often not fully enclosed by the varnish, which appears to have grown from the rock–soil–atmosphere contact upwards and downwards at the rock surface. Neighboring varnish samples partially had lichen growing on top. Most Californian samples were varnish-covered on their atmosphere facing side. The soil-facing side was usually covered by an orange-red coating. No preferred growth direction or starting point of varnish growth was observed.

Table 1 lists the specimens used for analysis together with information about the sampling location, the underlying rock type, and the varnish thickness

2.2. Sample preparation

Thick sections (about 70 μm thick) were prepared for EPMA and fs LA-ICP-MS measurements. For the EPMA measurements, the thick sections were polished, in contrast to the samples for the fs

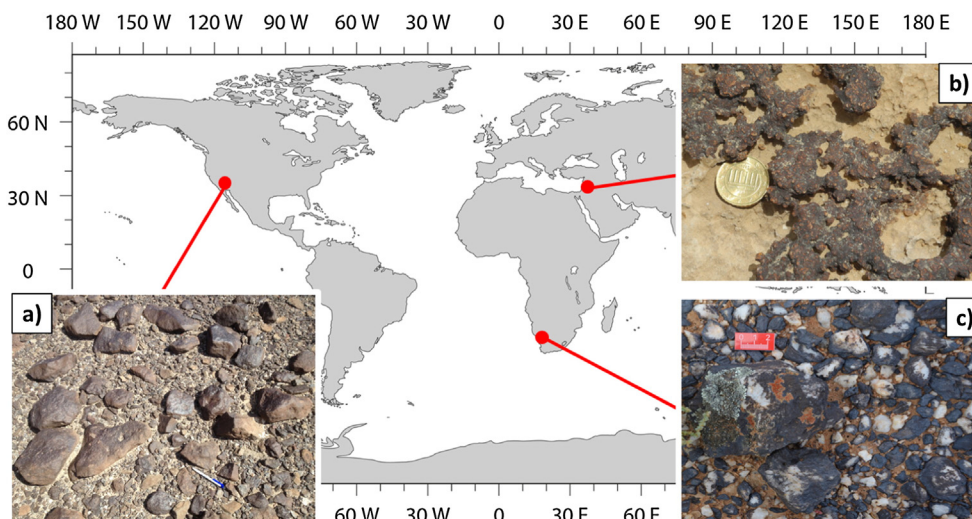


Fig. 1. Sampling locations of rock varnish, a) Mojave Desert, California, USA, b) Negev Desert, Israel, c) Knersvlakte, South Africa.

Table 1
Varnish samples with information about their sampling location, underlying rock type, and maximum varnish thickness.

Sample name	Country	Location	Rock type	GPS coordinates	Max. varnish thickness	Sampling	Lamination
IS13 V1 ^a	Israel	Negev Desert, Sde Boker	Quartz-rimmed limestone	30°52′25.13″N, 34°47′3.8″E	130 μm	Chip of a horizontal top of a boulder about 25 cm above the ground	Yes
IS13 V2a ^a	Israel	Negev Desert, Sde Boker	Quartz-rimmed limestone	30°52′25.13″N, 34°47′3.8″E	160 μm	Chip of a boulder about 50 cm above the ground	Yes
IS13 V3 ^a	Israel	Negev Desert, Sde Boker	Quartz-rimmed limestone	30°52′25.13″N, 34°47′3.8″E	250 μm	Chip of a boulder about 30 cm above the ground	Yes
IS13 V4 ^a	Israel	Negev Desert, Sde Boker	Quartz-rimmed limestone	30°52′25.13″N, 34°47′3.8″E	110 μm	From the ground	Yes
CA13 SWS1 ^b	California, USA	Mojave Desert, Stoddard Wells South	Dacite with sperulites	34°44′28.62″N, 117°4′10.14″W	60 μm	From the ground	Yes
CA13 SWW1 ^b	California, USA	Mojave Desert, Stoddard Wells West	Dacite with sperulites	34°45′13.8″N, 117°03′58.8″W	55 μm	From the ground	Yes
CA13 SWW3 ^b	California, USA	Mojave Desert, Stoddard Wells West	Dacite with sperulites	34°45′13.8″N, 117°03′58.8″W	50 μm	From the ground	Yes
CA13 SWW4 ^b	California, USA	Mojave Desert, Stoddard Wells West	Impure quartzite	34°46′19.74″N, 117°03′28.86″W	140 μm	From the ground	Yes
CA13 DV1 ^b	California, USA	Death Valley	Foid bearing andesite	36°21′16.798″N, 116°38′39″W	110 μm	From the ground	Yes
CA13 SCH45 ^b	California, USA	Mojave Desert, S of Death Valley Junction	Foid bearing andesite	36°11′51.3″N, 116°22′27.6″W	50 μm	From the ground	Yes
CA13 SS2 ^b	California, USA	Mojave Desert, Salt Spring	Impure quartzite	35°36′55″N, 116°38′39″W	70 μm	From the ground	Yes
CA WS-18 ^c	California, USA	Death Valley	Weathered magmatite		150 μm		Yes
CA14 JC-8 ^b	California, USA	Death Valley, Johnson Canyon	Spotted slate	36°05′49.87″N, 116°51′30.32″W	80 μm	From the ground	Yes
CA14 DV11 ^b	California, USA	Death Valley, near Scotty's Castle	Basanite	36°51′31″N, 117°15′59″W	60 μm	From the ground	Yes
SA10 #4 ^a	South Africa	Knersvlakte	Quartzite	31°16′45.2″S, 18°35′42.6″E	180 μm	From the ground	No
SA10 #8 ^a	South Africa	Knersvlakte	Quartzite	31°16′45.2″S, 18°35′42.6″E	180 μm	From the ground	No
SA10 #9 ^a	South Africa	Knersvlakte	Quartzite	31°16′45.2″S, 18°35′42.6″E	80 μm	From the ground	No
SA10 #12 ^a	South Africa	Knersvlakte	Quartzite	31°16′45.2″S, 18°35′42.6″E	300 μm	From the ground	No
SA13 mM-d ^a	South Africa	Knersvlakte	Quartzite	31°16′55.41″S, 18°35′17.8″E	120 μm	From the ground	No
SA13 mM-f ^a	South Africa	Knersvlakte	Quartzite	31°16′55.41″S, 18°35′17.8″E	250 μm	From the ground	No

^a Samples were provided and collected by Bettina Weber.

^b Samples were provided and collected by Meinrat O. Andreae.

^c Sample was provided by Tanzhuo Liu.

LA-ICP-MS determination of major and trace elements, where polishing was avoided to exclude trace-element contamination from the polishing material. The roughness of the unpolished surfaces can be neglected for fs LA-ICP-MS measurements because the pre-ablation step produced almost flat surfaces. Thin sections (25–30 μm) were prepared to determine the lithology of the underlying rocks. The varnish coatings were cut perpendicular to their layers (Fig. 2a), whereby cross-sections through the sedimentation sequence were exposed, similar to the procedure described by

Reneau et al. (1992). All thin and thick sections were prepared in an enclosing resin prior to thinning.

FIB slices, similar to those produced of rock varnish by Krinsley et al. (2013), were milled to sizes of about 50 × 30 μm and thicknesses of about 100–200 nm to perform X-ray micro-spectroscopy in transmission mode. For this purpose, micro-basins, which contain thicker varnish, were selected by microscopy (Fig. 2b), located by scanning electron microscopy (SEM) (Fig. 2c), and milled by a Ga⁺ ion beam (Fig. 2d).

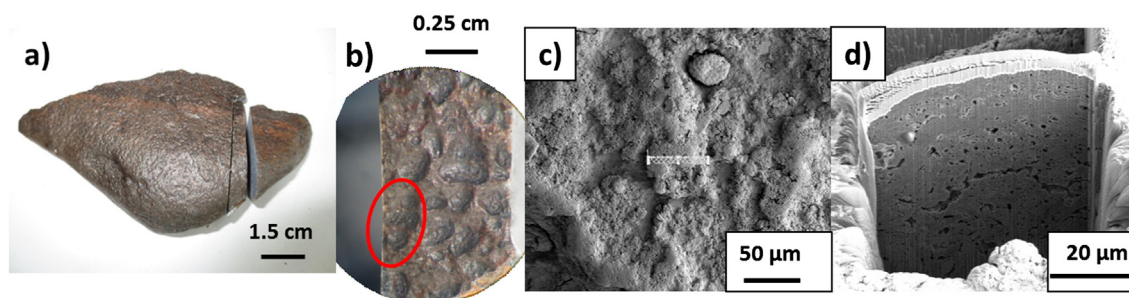


Fig. 2. Sample preparation, a) CA14-JC-8 sample, cut perpendicular to the varnish coating, b) Example of a micro-basin chosen on CA14-JC-8 for FIB preparation, c) FIB sampling location and area marked for Pt deposition and ion beam sputtering on sample SA13 mM-f, d) SA13 mM-f after FIB preparation, before liftout and thinning.

2.3. Imaging

A Leica DM RX polarizing microscope was used for the investigation of the varnish structure in thick sections and to observe ablated line scans subsequent to the analysis (Fig. 3). The underlying rocks and the approximate thicknesses of the varnish layers were determined by thin sections with a polarizing microscope. Pictures were taken of each thin and thick section, interesting sites were chosen and line scans were then performed on the thick sections with the fs LA-ICP-MS on these selected sites. Fig. 3 demonstrates the measurement procedure on a detailed image of two line scans, 40 μm and 10 μm wide, which were produced by fs LA-ICP-MS. Objectives from 1.6 to 100 were used for internal structure examinations (1–10 μm range) of varnish. Back-scattered electron images were recorded by EPMA, to visualize the samples by variations in back-scattering intensity resulting from differing atomic numbers, Z, displaying internal structures. Furthermore, prepared FIB slices were imaged by SEM, to allow the comparison of structures and element distribution by STXM–NEXAFS.

2.4. Femtosecond laser ablation-inductively coupled plasma-mass spectrometry

Measurements were carried out at the Max Planck Institute for Chemistry (Mainz, Germany). A combination of a ThermoFisher Element 2 single-collector sector-field ICP-mass spectrometer and an ESF fs laser ablation system NWRFemto with a wavelength of 200 nm, producing laser pulses at 150 fs, was used. The fs LA-ICP-MS is especially suitable for the analysis of small sample amounts (Macholdt et al., 2014) and has the advantage of an almost matrix-independent calibration (Jochum et al., 2014). Important parameters of the ICP-MS and the lasers are listed in Tables 2 and 3. Laser ablation was conducted in a New Wave Large Format Cell in a He atmosphere. This carrier gas was mixed with an Ar gas flow to transport the aerosols generated by ablation. The washout time was about 30 s and the blank count rate was determined prior to each ablation for about 15 s.

A new ThermoFisher medium mass resolution mode (2000) with flat top peaks was chosen for all measurements, since in this way many oxides and molecules from Ar, O, and the major compounds of varnish produced in the plasma can be separated from the ions, giving an improvement of the signal to blank ratio for many elements.

After pre-ablation, each sample was scanned along a profile from the underlying rock through the varnish into the embedding resin. The

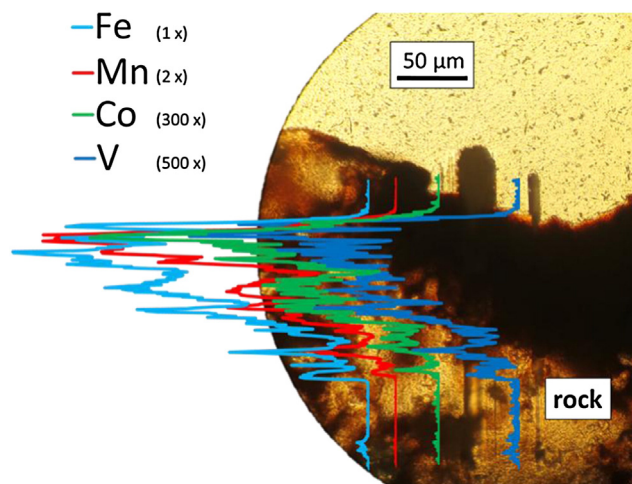


Fig. 3. Thick (~70 μm) section of sample IS13 V2a imaged by microscopy with tracks from two LA-ICP-MS line scans (40 μm and 10 μm wide lines). The image shows the results of the measurements along the narrower scan line. The graphs are not to scale to allow comparison. The factors with which the element abundances were multiplied are 2 for Mn, 300 for Co, and 500 for V.

Table 2

Operating parameters used for the fs laser ablation system.

	NWRFemto
Laser type	Ti:sapphire
Wavelength [nm]	200
Pulse length [fs]	150
Energy density [J cm^{-2}]	0.8
Spot size [μm]	10 (fast scan), 40 (slow scan)
Pulse repetition rate [Hz]	50
Scan time [s]	250, 350
Scan speed [$\mu\text{m s}^{-1}$]	1 (slow scan), 5 (fast scan)

varnish region was defined by high ($\geq 2\%$) MnO_2 abundances. Measurements with exceptionally low count rates for all elements, an indicator for holes and cracks, were excluded. To obtain a representative bulk analysis for the varnish, the concentration for each measurement was averaged over the profile from the underlying rock contact to the resin. Bulk analyses were performed for the major elements (Na, Mg, Al, Si, P, K, Ca, Ti, Mn, Fe) and 24 trace elements (isotopes used are listed in Appendix A) with a scan speed of 1 $\mu\text{m s}^{-1}$, a spot size of 40 μm and a time per pass of about 0.8 s, using a combination of magnetic and electrical scan modes. Adjacent to these measurements, higher resolved profile measurements of the “neighboring” elements with similar atomic masses, V, Cr, Mn, Fe, Co, Ni, and Cu, could be performed using solely the fast electrical scan mode. In this case, a scan speed of 5 $\mu\text{m s}^{-1}$ and a spot size of 10 μm were chosen. Since no suitable micro-analytical varnish reference material exists, the homogeneous GSE-1G glass (GeoReM database <http://georem.mpch-mainz.gwdg.de>) with high trace element contents (ca. 500 $\mu\text{g g}^{-1}$) and a basaltic matrix with 12.7% FeO and 590 $\mu\text{g g}^{-1}$ Mn was used for calibration. It is applicable due to the nearly matrix-independent calibration for fs LA-ICP-MS.

The element concentrations were determined by measuring the ion intensities of the elements of interest using Al as the internal standard (analogous to Goldsmith et al. (2014)). This element was measured by EPMA on three to nine varnish samples from each location, analyzing 11–16 spots per sample. For further correction, a total oxide content of about 95% was assumed, which was obtained from the EPMA results of the samples. However, the concentrations of the higher-resolved profile measurements by fast electrical scans are less precise, since no internal standard with constant amounts throughout the profiles was available and no total oxide content could be assumed.

The concentration of an element of interest, EL, (m_{fEL}) was calculated by a procedure described in Jochum et al. (2007). The precision (RSD) of the fs LA-ICP-MS data, determined by three independent analyses of the homogeneous GSE-1G glass, was about 3%. However, due to the large sample heterogeneity, it was much higher for the bulk varnish analyses, determined by 12–30 independent analyses on each sample at different locations, and varied between 25 and 80%. The measurement accuracy, defined as the overall analytical uncertainty at the 95% confidence level, is listed for each element in Appendix A. It was about 35% for most elements. The detection limits, DLs (defined as three times the standard deviation of the blank values), are listed in Table 4. The DLs ranged between <0.01–1100 $\mu\text{g g}^{-1}$ and 1–26 $\mu\text{g g}^{-1}$ using spot

Table 3

Operating parameters of the Element2 ICP-MS.

rf power [W]	1270
Cooling gas flow rate [l min^{-1}]	15
Auxiliary gas flow rate [l min^{-1}]	1
Carrier gas (Ar) flow rate [l min^{-1}]	0.8
Carrier gas (He) flow rate [l min^{-1}]	0.7
Sample time [s]	0.002
Samples per peak	25
Mass window [%]	40
Time per pass [s]	0.2 (fast scan), 1.4 (slow scan)
Mass resolution	2000

Table 4

Detection limits of the fs LA-ICP-MS analysis. Data were evaluated from blank measurements without sample material (DL = three times the variability of the blank). A: spot size = 40 μm ; scan speed = 1 $\mu\text{m s}^{-1}$ (slow line scan); B: spot size = 10 μm ; scan speed = 5 $\mu\text{m s}^{-1}$ (fast line scan).

A		B	
[$\mu\text{g g}^{-1}$]	[ng g^{-1}]	[$\mu\text{g g}^{-1}$]	
Na	150	La	7
Mg	25	Ce	80
Al	160	Pr	16
Si	1100	Nd	80
P	70	Sm	<0.01
K	50	Eu	<0.01
Ca	320	Gd	55
Ti	7	Tb	13
Mn	20	Dy	<0.01
Fe	90	Ho	<0.01
Co	1	Er	<0.01
Ni	40	Tm	<0.01
Rb	0.8	Yb	<0.01
Sr	0.7	Lu	<0.01
Y	0.3	Pb	60
Cs	0.8	Th	5
Ba	0.4	U	5
		V	1
		Cr	5
		Mn	5
		Fe	30
		Co	1
		Ni	20
		Cu	5

sizes of 40 μm and 10 μm and scan speeds of 1 $\mu\text{m s}^{-1}$ and 5 $\mu\text{m s}^{-1}$, respectively (Table 4).

2.5. Electron probe microanalysis

Quantitative measurements of major element concentrations were conducted at the Institute of Geosciences at the Johannes Gutenberg University (Mainz, Germany) using a JEOL JXA-8200 electron microprobe. The samples were diamond-polished, cleaned with petrol ether in an ultrasonic bath and kept dry in a vacuum furnace before being coated with ~20 nm of thermally evaporated carbon. The microprobe was operated at an accelerating voltage of 15 kV, a beam current of 12 nA and a beam diameter of 2 μm . Five wavelength dispersive X-ray spectrometers (WDS) were used to measure K α lines of Mn, Na, Al, Cr, Fe, Mg, Ti, K, Ca, and Si with peak counting times of 20 s. Natural and synthetic phases (NaAlSi₃O₈, Al₂O₃, Cr₂O₃, Fe₂O₃, MgO, MnTiO₃, KAlSi₃O₈ and CaSiO₃) were utilized as reference materials and for instrument stability monitoring. For data correction the Phi-rho-z method based on the CITZAF correction (Armstrong, 1991) was applied.

2.6. Scanning transmission X-ray microscopy–near edge X-ray adsorption fine structure spectroscopy and focused ion beam sputtering

Focused ion beam (FIB) sputtering (milling) was performed at the Max Planck Institute for Polymer Research (Mainz, Germany) using a Nova600Nanolab FIB dual-beam instrument of FEI. Simultaneous SEM microscopy was used to carefully determine and monitor the site of milling. Selected micro-basins were used for the preparation of the 50 \times 30 μm FIB slices. The samples were sputtered with Pt using Baltec MED020 sputtering equipment to avoid charging effects during electron- and ion radiation, and to acquire a stable image. Subsequent to sputtering the whole sample with a 50 nm thick Pt coating, preparation sites were coated with an additional Pt layer, about 2 μm thick, using beam-induced Pt deposition from a metallo-organic precursor gas (1 nA at 30 kV). Milling was performed by Ga⁺-ion sputtering with a resolution of about 10 nm. In a first milling step (20 nA, 30 kV), two trenches on both sides of the Pt deposition were created, followed by a second milling step at lower beam currents (7 nA and 5 nA at 30 kV) to receive flat surfaces of the pre-thinned, about 1 μm thick, lamella. After liftout, the samples were transferred to a TEM grid and were attached onto it with a small Pt spot. Stepwise thinning and polishing at further reduced ion beam currents (1 nA and 0.5 nA at

30 kV) produced lamellae with thicknesses of about 100–200 nm. These thin slices and the transfer onto a TEM grid are necessary for measurements by the STXM.

The STXM–NEXAFS analysis was conducted using two X-ray microscopes: (i) the X-ray microscope at beamline 5.3.2.2 (Kilcoyne et al., 2003) at the Advanced Light Source, Berkeley, CA, USA and (ii) the MAXYMUS microscope at beamline UE46-PGM-2 (Follath et al., 2010) at the synchrotron BESSY II, Helmholtz-Zentrum Berlin, Germany. Both STXM instruments are equipped with a high energy resolving grating (resolving power at the carbon K-edge: ALS E/ Δ E \leq 5000; BESSY II: E/ Δ E \leq 8000), a Fresnel zone plate, providing a spatial resolution of about 30 nm, and phosphor-coated Lucite photomultiplier tubes for the detection of transmitted photons. In this study, STXM elemental maps of certain elements of interest (i.e., Fe, Mn, Ca, and C) are presented, which have been recorded as images at discrete energies. Data were evaluated with the Interactive Data Language (IDL) widget “Analysis of X-ray microscopy Images and Spectra” (aXis2000) and the overlay images (Fig. 10) produced by Adobe Photoshop CS6.

3. Results and discussion

3.1. Imaging

Microscopic investigations revealed that the maximum thicknesses of the coatings, deposited on different underlying rock types varied between 50 and 300 μm (see Table 1). They also show that the varnish covers topographical highs of the sample surfaces, but is thicker in the micro-basins (Liu and Broecker, 2013). The varnish material fills cracks and fissures, intruding into the underlying rocks.

Internal structures of the varnish coatings were studied for comparison and characterization. Since these structures are μm to nm in size, they were visualized by the highly resolving techniques of SEM, using backscattered electron (BSE) images on FIB slices, and EPMA, on thin sections. In the microscopic view, cross sections of the South African varnishes revealed stromatolitic structures (Fig. 4a), rock varnish features observed before (Perry and Adams, 1978). Mineral grains up to 70 μm in size and cavities were identified within the South African varnish coating SA13 mM-f (Fig. 4b). Furthermore, up to 10 μm large mineral detritus, enveloped in depressions between protrusions of the stromatolitic features, were observed, similar to those described by Perry and Adams (1978) and Dorn et al. (2013) in detail. The underlying rocks of the South African samples are quartzite pebbles. The rocks underneath the varnish coatings collected in Israel are limestones with significant amounts of diatom fossils and varying amounts of quartz minerals. At the surface, in direct contact with the varnish, the calcite had been dissolved, leaving a SiO₂ rich, insoluble matrix. The Israeli varnish has an orange to black and brown color and shows cauliflower shaped internal structures (Fig. 4a). Mineral grains, which are only a few micrometers in size, are incorporated in the varnish coatings IS13 V3 and V1. Close to the contact with the coating, cavities are present within the varnish and the underlying rock (Fig. 4c, d). These cavities and mineral grains can also be observed in the Californian varnish coating CA14 JC-8 (Fig. 4f). The Californian coatings are dark brown and have smooth surfaces. Sample CA13 DV1 displays a wavy internal varnish structure in contact with the underlying rock, which is covered by flat deposits (Fig. 4e). The interpretation provided by Reneau et al. (1992), who suggested a higher trapping efficiency and higher accretion rates for rougher, lower surfaces, which decrease to the top, producing smoother surfaces over time, seems suitable to these observations. The Californian samples exhibit multiple underlying rock types, magmatites, metamorphites, and sediments (see Table 1). All varnish coatings contain cavities and cracks, but while the cavities are <0.5 μm for the Israeli and Californian samples, they can be up to 1 μm large in the South African samples. However, it cannot be excluded that the cracks are partially preparation artifacts.

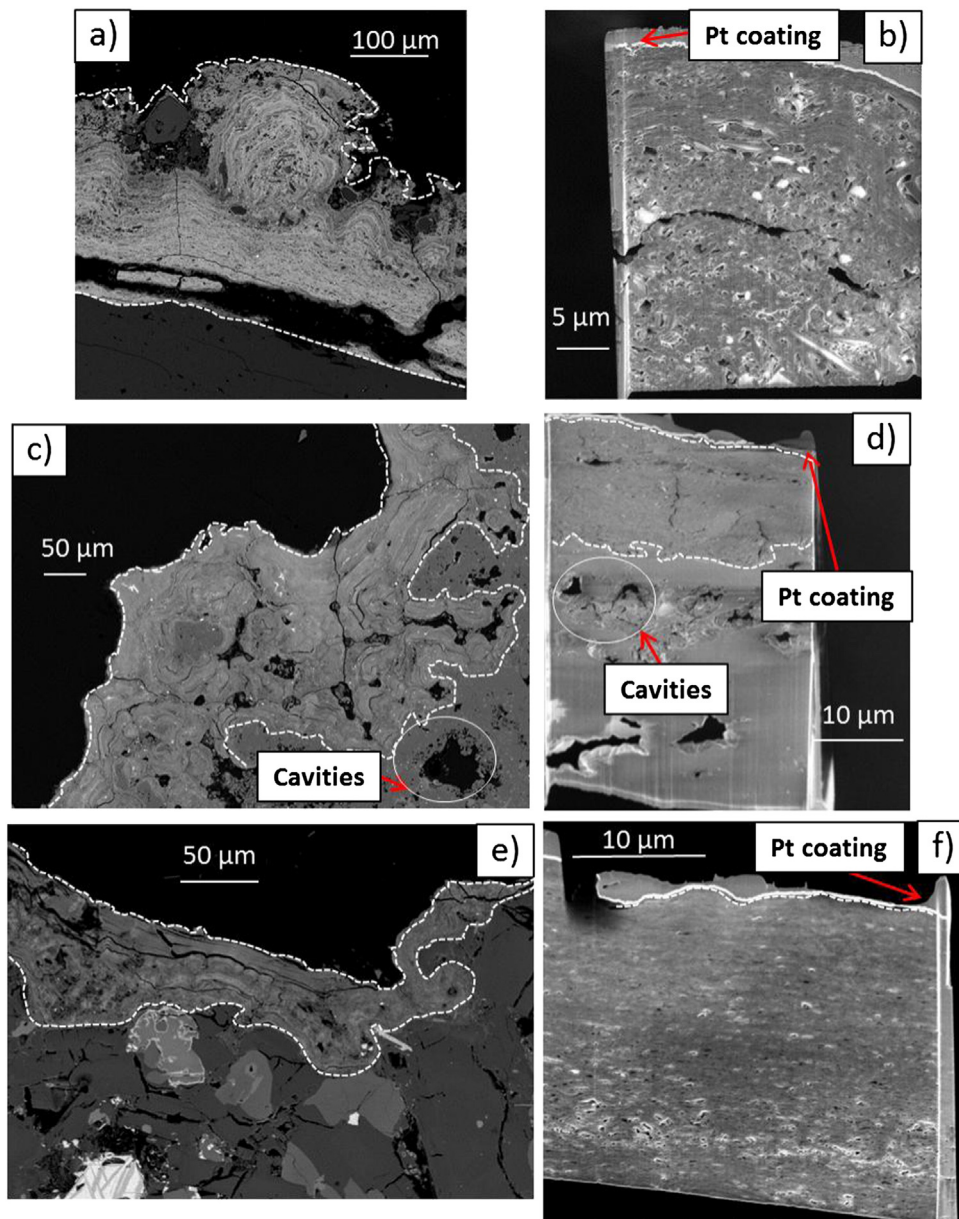


Fig. 4. a), c), e): Backscattered electron (BSE) images of varnish thick sections, revealing structures with differing average atomic numbers, Z, a) SA13 mM-f, c) IS13 V3, e) CA13 DV1. All BSE images were taken by an EPMA with an accelerating voltage of 15 kV and a beam current of 12 nA. Images b), d), f) are SEM images of FIB slices, revealing topographic structures, such as cracks, holes, and mineral inclusions, with b) SA13 mM-f, d) IS13 V1, and f) CA14 JC-8. All SEM images were produced by an FIB instrument with an accelerating voltage between 2 and 5 kV. All FIB slices had been coated on their top side by Pt, which is imaged as a light line on top of the samples and the gray matrix above. Rock-to-varnish and varnish-to-Pt boundaries are marked by white, dashed lines.

3.2. Major and trace element determination by fs LA-ICP-MS

3.2.1. Bulk analysis of major and trace elements

Appendix A shows the average analytical results for each sample. Some characteristic element enrichments are plotted in Fig. 5, where the values are normalized to those of the upper continental crust (Rudnick and Gao, 2003) and arranged approximately according to decreasing enrichments in the varnish samples. In addition to the high Mn concentrations, Pb, Co, Ce, Ni, and Ba are also enriched in all varnish samples. High Ba values have also been observed by Garvie et al. (2008). Barium is known to be capable of incorporation into manganese oxihydroxide structures, e.g., in hollandite (Post, 1999). The high enrichment of Ni, Co, and Pb is presumably due to the high adsorption potential of the Mn oxihydroxides (Thiagarajan and Lee, 2004). The source of these elements might be dust that was leached by rain or dew

(Thiagarajan and Lee, 2004). An atmospheric contribution to the varnish genesis was previously verified for Pb, Hg (Nowinski et al., 2010; Nowinski et al., 2013), and ^{210}Po (Hodge et al., 2005) enrichments in the outer varnish layers, elements that were emitted by nuclear testing sites, coal-fired power plants and smelters. The enrichments in Ce, also observed in the REE patterns as positive Ce anomalies (Fig. 6), may be caused by the change from a REE-leaching reducing environment (Ce^{3+}) to an oxidizing environment (Ce^{4+}) where Ce(IV) can precipitate or be adsorbed to $\delta\text{-MnO}_2$ or Fe oxihydroxides (Ohta and Kawabe, 2001). It strengthens the hypothesis of an aqueous atmospheric deposition as a source of these elements, previously suggested for varnish samples from the Mojave Desert and Death Valley (Thiagarajan and Lee, 2004), it might be an indicator for direct oxidation of Ce by birnessite (Post, 1999) or for the role of Mn-oxides as repositories of trace elements presumably derived from atmospheric aerosols (Garvie

et al., 2008). A positive correlation between Mn and Ce was observed for all Californian and Israeli varnish samples. However, no correlation was present for any South African varnish sample.

The element abundances agree well with literature values of rock varnish (Fig. 5, gray shaded area) published for California (Thiagarajan and Lee, 2004), Utah (Wayne et al., 2006), Nevada (Wayne et al., 2006) and Israel (Goldsmith et al., 2014). However, not all element values were provided by the manuscripts, hindering a direct comparison. The enrichments of most elements are similar, with some exceptions, such as Ti, Al, and Mg, for which few literature values are provided in these manuscripts. The differences between the Israeli and the Californian samples of this work are mostly restricted to the elements Ni and Pb, while the South African samples differ from the other locations with regard to several elements, such as Mn, Co, Ce, and Ba (Fig. 5). The Californian samples were subdivided into two groups, California A (CA WS-18, CA13 SS2, CA13 SCH45, CA13 DV1) and California B (CA13 SWS1, CA13 SWW1, CA13 SWW3, CA13 SWW4), depending on their major and trace element composition (see Appendix A). Interestingly, no chemical difference can be seen between the Israeli samples that showed different macroscopical surface structures (smooth and botryoidal). The REE results (Fig. 6) were normalized to a chondritic composition, and display positive Ce and negative Eu anomalies in all samples. The REE patterns of the samples from Israel and California are very similar, enriched in light REE ($La_N/Yb_N = 11-12$) and with significant positive Ce anomalies ($Ce/Ce^* = 2.1-5.3$). The South African samples have significantly lower light REE contents ($La_N/Yb_N = \sim 3.5$) and less positive Ce anomalies ($Ce/Ce^* = \sim 1.5$) than the other samples. The negative Eu anomaly is of about the same order for all samples ($Eu/Eu^* = 0.6-0.7$). The ratios of Mn/Fe (3.1–25.1 South Africa, 0.4–0.6 Israel, 0.3–1.2 California A and 0.9–2 California B), Mn/Ba (112–170 South Africa, 5–9.9 Israel, 12–28 California A and 4–11 California B), Ni/Co (0.03–2.1 South Africa, 1.1–1.8 Israel, 0.4–0.7 California A and 0.2–0.4 California B) and Pb/Ni (1.1–1.3 South Africa, 0.4–0.8 Israel, 4–13 California A, and 4–23 California B) exhibit strong variations between different locations. Fig. 7 demonstrates that these ratios are suitable for distinguishing between the locations of the varnish samples analyzed in this work. Possible reasons for these differences might be differing genesis, but also diverging dust source compositions, ages, climates,

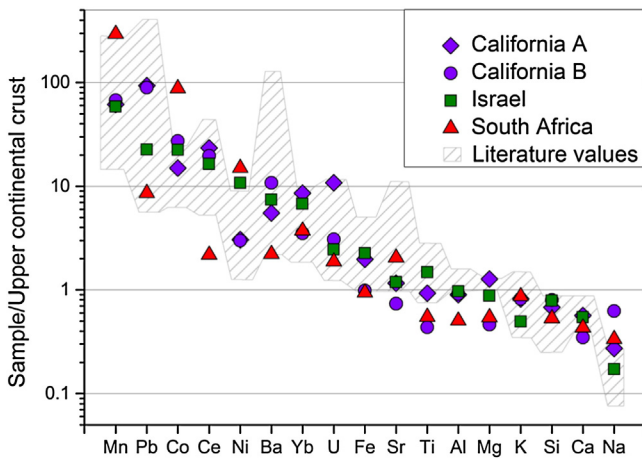


Fig. 5. Element abundances normalized to the values for the upper continental crust (Rudnick and Gao, 2003). Displayed are the enrichment factors of selected elements in the varnish. Elements are arranged approximately according to decreasing enrichment in the varnish samples. The differences between the Israeli samples and the Californian samples are most striking for the elements Ni and Pb, while the South African samples deviate for several elements, such as Mn, Co, Ce, and Ba. Within the Californian samples one can distinguish between the mean results of the samples CA WS-18, CA13 SS2, CA13 SCH45 and, CA13 DV1 (California A) and those of the samples CA13 SWS1, CA13 SWW1, CA13 SWW3 and CA13 SWW4 (California B). The gray shaded area represents the range of literature rock varnish values (Thiagarajan and Lee, 2004; Wayne et al., 2006; Goldsmith et al., 2014).

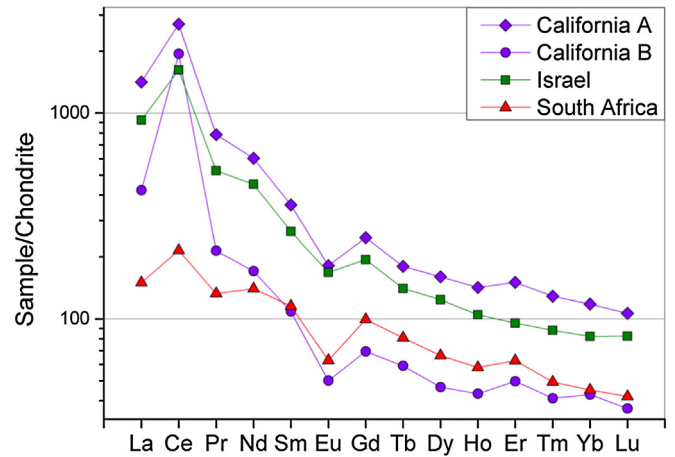


Fig. 6. Chondrite-normalized REE concentrations in the varnish samples. The patterns show a distinct positive Ce anomaly and a negative Eu anomaly. The samples from Israel and California are very similar, enriched in light REE ($La_N/Yb_N = 11-12$) and with a significant positive Ce anomaly ($Ce/Ce^* = 2.1-5.3$). The South African samples have lower light REE enrichments with $La_N/Yb_N = \sim 3.5$ and less positive Ce anomalies ($Ce/Ce^* = \sim 1.5$) than the other samples. The negative Eu anomaly is similar for all samples ($Eu/Eu^* = 0.6-0.7$).

rain or dew amounts or pH conditions during their growth, or even a combination of them (Engel and Sharp, 1958; Broecker and Liu, 2001).

Literature rock varnish element ratios from California, Nevada and Utah (Thiagarajan and Lee, 2004; Wayne et al., 2006) fall into the range of the Californian and Israeli rock varnish ratios from our studies. Interestingly, literature element ratios falling into the range of this studies Israeli rock varnish samples are without exception samples collected in the Cima volcanic field in the Mojave Desert (Thiagarajan and Lee, 2004). Literature values from the Death Valley (Thiagarajan and Lee, 2004), Nevada (Wayne et al., 2006) and Utah (Wayne et al., 2006) plot in the fields of this studies Californian rock varnish element ratios.

3.2.2. Profiles

Profile patterns of Mn and Fe within varnish have been used by some authors as paleoclimate reconstruction tools (Liu and Dorn, 1996), where Mn rich (25–45% MnO) layers are interpreted as wet periods, Mn poor layers (5–15% MnO) as dry periods, and layers containing moderate amounts of Mn (15–25% MnO) as periods of climatic transition between extremely dry and extremely wet conditions

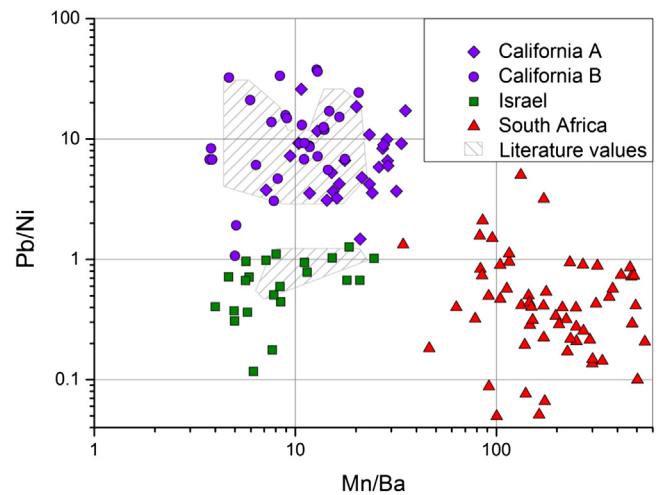


Fig. 7. Pb/Ni vs. Mn/Ba values for the three sampling locations. The data for the different sampling locations plot well separated from each other and can therefore be easily distinguished. The gray shaded area represents the range of literature rock varnish values (Thiagarajan and Lee, 2004; Wayne et al., 2006).

(Dorn, 1984; Liu and Broecker, 2013). However, these layers are extremely thin and only longer wet or dry periods can be detected by fs LA-ICP-MS with its spatial resolution of 10 μm .

Therefore, 7 to 15 high resolution MnO_2 and Fe_2O_3 profile measurements were conducted on each varnish thick section (Fig. 3). The profile patterns vary within each sample, a variation that might be influenced by the deposition process, but also by sample inhomogeneities, such as thickness differences, cavities, and mineral grain inclusions (see Fig. 4). Although there is a large scatter in the profile measurements, it is insignificant compared to the differences between the three sampling locations. This is shown in Fig. 8, where for each location one profile is plotted, representing a “typical” profile of the location (Fig. 8a, b, d). Most of the measured values of rock and resin are left out for clarity. Fig. 8c shows the values for the $\text{MnO}_2/\text{Fe}_2\text{O}_3$ ratios, which differ significantly for the different locations. Typically ratios are <1 for Californian and Israeli samples for most parts of the profiles, and 10–200 for the South African samples, with variations within the profiles.

The typical Californian profile (Fig. 8b) shows a high Fe abundance (about 20%) close to the underlying rock, with MnO_2 concentrations of about 2%. About 20 μm closer to the rim, or varnish surface, the MnO_2 and Fe_2O_3 amounts rise, forming small plateaus with about 4% MnO_2 and 45% Fe_2O_3 (no. 1 in Fig. 8b). About 5 μm further outward the Fe_2O_3 concentration rises to 50% and the MnO_2 concentration increases significantly to 25% (no. 2 in Fig. 8b). At the outer rim of the varnish, MnO_2 and Fe_2O_3 have approximately the same abundance, with high Fe_2O_3 and MnO_2 concentrations of up to 50% (no. 3 in Fig. 8b).

The Israeli samples (Fig. 8c) show variations of the MnO_2 values with significant peaks for Mn and Fe. They reveal a higher total value of Fe_2O_3 throughout the profiles than the Californian samples. Manganese and Fe show common highs for some peaks, but for others, especially in the youngest and oldest varnish layers, Fe is enriched without a simultaneous Mn enrichment at the same location. The South African profiles

(Fig. 8a) show significantly higher abundances of MnO_2 compared to Fe_2O_3 . The $\text{MnO}_2/\text{Fe}_2\text{O}_3$ ratios are about 40 (Fig. 8d), and for some samples even up to 180 (not displayed). These profiles show no recurring peaks at the same distances from the rim that could be used as paleoclimate indicators. The profile patterns here might mostly depend on mineral inclusions and cavities, both of which are highly abundant in the South African samples (Fig. 4a, b). These South African rock varnish samples show therefore no internal Mn–Fe-rich VMLs (varnish microlaminations).

3.3. Major element analysis by electron probe microanalysis

The spatial resolution of the electron probe microanalysis is higher ($\sim 2 \mu\text{m}$) than that of the fs LA-ICP-MS (10–40 μm). Since solid and homogeneous areas with few mineral grains or cavities were analyzed by EPMA, the results represent the composition of areas containing more cementing material, which is enriched in MnO_2 . The data, therefore, show significantly higher MnO_2 values than those obtained by fs LA-ICP-MS (Fig. 9, Table 5). However, the values of both analytical methods from the same varnish sample lie on the same trend line in a MnO_2 vs. SiO_2 plot. These plots suggest linear mixing series between Mn/Fe oxide-rich components and Mn-free silicate end members for each sample. The correlation lines converge towards a similar SiO_2 content for the Mn-free end members, in the range of average dust compositions (50–75%, Moreno et al., 2006; Castillo et al., 2008). The individual end member values may be characteristic for the composition of the dust involved (Fig. 9). This value is lower for the Israeli samples (about 50% SiO_2) than for the South African and Californian varnish samples (about 60–65% SiO_2). A reason for this difference might be a SiO_2 -poor dust composition of the Israeli varnish source. Recent Israeli dust has SiO_2 amounts of about 38% (Goldsmith et al., 2014), while recent air-borne material from the Coxcomb Mountains has much higher SiO_2 values of approximately 51% (Engel and Sharp, 1958). There is no

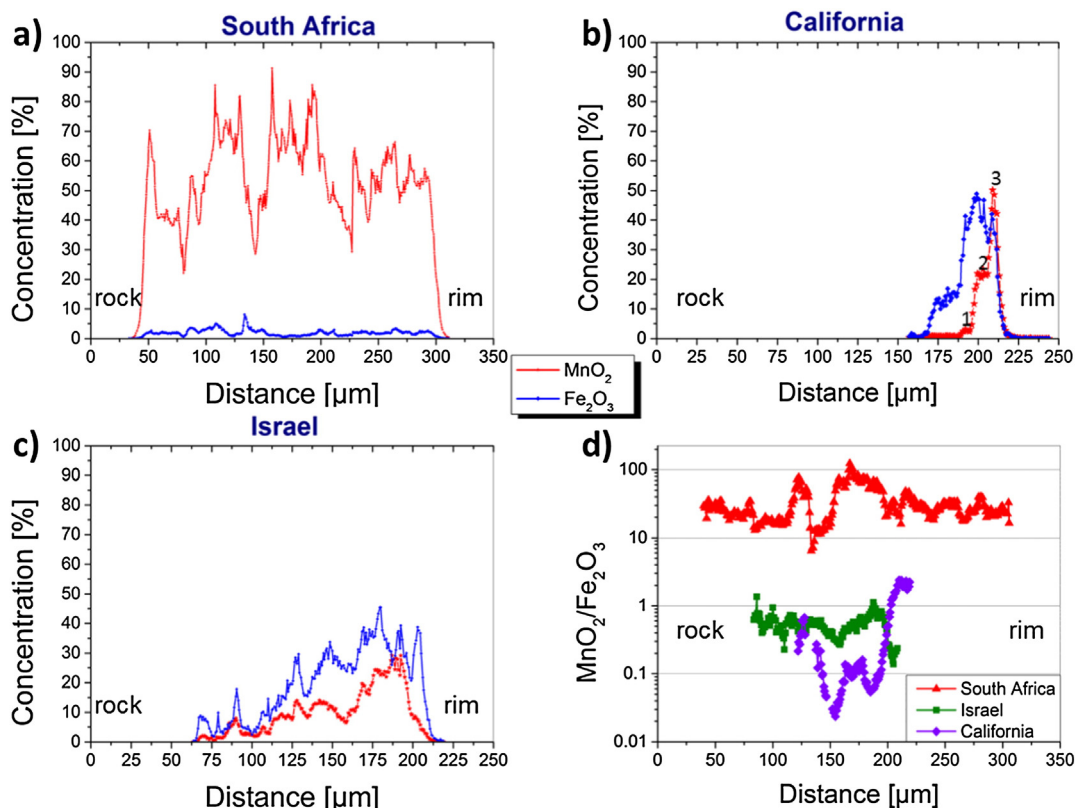


Fig. 8. Typical profiles of a) South African, b) Californian, and c) Israeli varnish samples are plotted with their MnO_2 and Fe_2O_3 concentrations. d) displays the $\text{MnO}_2/\text{Fe}_2\text{O}_3$ ratios of profiles a), b), and c). All measurements were performed by fs LA-ICP-MS with a scan speed of $5 \mu\text{m s}^{-1}$ and a spot size of 10 μm .

indication for a relationship between the SiO₂ content of the end member and the SiO₂ value of the underlying rock (Fig. 9), in contrast to the conclusions stated by Engel and Sharp (1958). This is especially obvious for the samples IS13 V1 and SA13 mM-f, where the quartzite in contact with the coating has a composition of almost 100% SiO₂.

3.4. Element distribution maps

For each location, one or two samples were prepared as ultra-thin FIB slices to analyze the distribution of certain elements and molecules (i.e., Mn, Fe, Ca, and CO₃²⁻) in the varnish at the nm scale by STXM-NEXAFS. Since the NEXAFS spectra at the X-ray absorption edge are specific to functional groups and bonding states, C-, N-, and O-NEXAFS spectra were measured in addition. These elements and their bonding types can be indicators of a biological origin. A systematic investigation of the NEXAFS spectroscopy will be the focus of a future study. An organic carbon signal was detected in all samples, but no significant N was found in any mapped area. This might be an indicator for the absence of living matter, but N might also have been leached by water in strongly decomposed biological matter, or it might even be present in concentrations below the detection limit of STXM (1–3 mol% in humic substances in soil). CaCO₃ was excluded as a possible C-phase by selective measurements of CO₃²⁻ for each sample.

Fig. 10a displays the enrichment of Fe and Mn in a cross section through the varnish layer of the Israeli sample IS13 V1. Manganese and Fe show distinctive layers throughout the coating (at scales of about 100–500 nm), running parallel to the rock surface. This feature can be interpreted as an indicator for the sedimentary origin of the coating and the thin layers are similar to those observed by Liu and Broecker (2013), which were used for paleoclimate reconstruction. Some larger Ca-containing mineral grains (~500 nm) are mapped in sample IS13

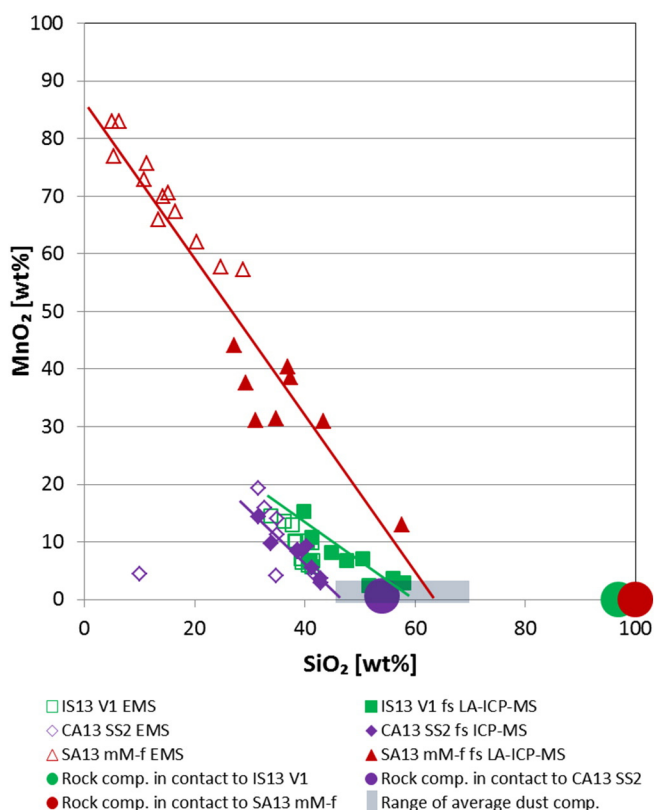


Fig. 9. EPMA and fs LA-ICP-MS MnO₂ vs. SiO₂ plots with trend lines for one sample from each sampling location. No indication of a relationship between the SiO₂ concentration of the manganese free end member and that of the rock in contact to the varnish is evident. All plots converge towards SiO₂ values in the range of average dust compositions (Moreno et al., 2006; Castillo et al., 2008).

V1 (Fig. 10a), whereas cavities are rare in this sample. The dense structure of the Israeli sample is pervaded by cracks and fissures compared to varnish from other locations (Fig. 10b, c). Carbon in the Israeli sample IS13 V1 is mostly present as a lining of cavities underneath the varnish crust in the underlying rock, and along the cracks and fissures within the varnish (Fig. 10d). This feature is distinct from the samples collected in California (Fig. 10e) and South Africa (Fig. 10f), where carbon occurs in layers or chaotic patterns.

The cavities in the underlying rock of sample IS13 V1 also show linings of Mn and Fe, and similar cavities were also observed in the Californian FIB slice, with similar element abundances (Fig. 10 g). These cavities are of specific interest, since they occur in a quartz rich limestone (IS13 V1), as well as in a basaltic rock (CA14 DV11). Their genesis might be similar to the submicron deposited Mn–Fe skins described by Garvie et al. (2008), subsequent to mineral decay in the less stable underlying rocks (Dorn et al., 2013), and is referred to as case hardening (Dorn, 2008).

The Californian samples display homogeneously distributed cavities inside the varnish (Fig. 10c) similar to those observed by Krinsley et al. (2013). In sample CA14 JC-8, Fe-containing minerals were mapped in some of these cavities which were a few hundred nanometers in size and are displayed as green areas (Fig. 10c). In the varnish FIB samples CA14 JC-8 and CA14 DV11, Mn and Fe show distinct layers parallel to the rock surface (Fig. 10c and g), similar to the layering previously observed in a FIB slices of a Death Valley sample (Krinsley et al., 2013) and furthermore used as paleoclimate reconstruction tools (Perry and Adams, 1978). A carbon-rich band, ~1 μm thick, is evident in the ultra-thin section of sample CA14 JC-8 (Fig. 10c, e). In the lower part of this sample, C is present as thin (~100 nm) rippled layers or chaotic structures (Fig. 10e). These bands are layers with higher abundances of organics, which could be residues of organisms that grew on the former varnish surfaces, as proposed by Wang et al. (2011), or organic-rich dust that was deposited with the sedimentation process, and that was incorporated during the varnish genesis.

The South African sample SA13 mM-f contains numerous large (up to 5 μm long) mineral grains, many of them containing Fe (Fig. 10b, h). Large cavities of several μm are irregularly distributed throughout the sample. Structures defined by elevated Fe and Mn contents are present, but seem to be mainly an effect of density variations rather than compositional differences. Calcium is enriched in the upper part of the FIB slice as layers, following a cauliflower-like structure (Fig. 10 h) similar to those observed in rock varnish FIB slices before (Krinsley et al., 2013). Carbon is present throughout the sample, but is especially enriched in the lining of cavities (Fig. 10f). A possible interpretation is that the cavities were formerly filled by organic material that decayed leaving cavities with organic C signatures at their rims.

3.5. Structures at the nm to μm scale

The combination of different analytical techniques at different scales demonstrates considerable variability within the coatings. The techniques used were the fs LA-ICP-MS with 10–40 μm spatial resolution, the EPMA with 2 μm resolution, and the STXM-NEXAFS with a resolution of about 30 nm. Layerings in the Israeli and Californian rock varnish samples can be observed at each scale, with the thinnest detected Mn layers in the 100–500 nm range. These layers have similar extensions to those observed by Liu and Broecker (2013), who interpreted them as indicators for climate fluctuations and as a paleoclimate reconstruction tool for the Quaternary period. A layer of 100–500 nm thickness could represent an age interval of about 100–500 years, assuming a growth rate of 1 μm per 1000 a. These intervals are in the range of typical climate fluctuations during the Holocene.

The Israeli and Californian samples seem very similar regarding their elemental composition at the 10–40 μm scale, but differ for selected elemental abundances, such as Ni and Pb (Fig. 7). The Californian samples can furthermore be subdivided into California A and B, based on their

Table 5
Concentrations of major elements in the varnishes, obtained by EPMA measurements.

	Na ₂ O	SiO ₂	K ₂ O	TiO ₂	Fe ₂ O ₃	Al ₂ O ₃	MgO	CaO	Cr ₂ O ₃	MnO ₂
SA10 #4 [wt %]	0.97	17.40	2.32	0.20	4.69	8.29	1.06	0.60	0.04	54.09
RSD [%]	28	46	15	52	52	39	24	13	59	23
SA10 #8 [wt %]	1.47	9.52	3.51	0.07	2.58	4.27	0.88	0.38	0.05	71.51
RSD [%]	9	40	11	71	45	41	32	19	76	11
SA13 mM-d [wt %]	0.83	10.29	2.44	0.11	3.52	5.95	1.99	1.58	0.04	60.07
RSD [%]	23	59	14	77	56	57	15	16	47	21
SA13 mM-f [wt %]	0.96	14.35	3.73	0.05	2.24	3.39	0.82	0.43	0.03	68.50
RSD [%]	29	52	13	68	50	49	38	34	87	15.12
Average South Africa [wt %]	0.91	12.29	3.05	0.10	3.01	5.73	1.26	1.11	0.03	63.56
RSD [%]	33	30	21	46	29	32	42	51	36	12
CA13 SWW1 [wt %]	0.37	33.32	1.92	0.44	10.80	19.56	2.16	0.84	0.04	18.04
RSD [%]	50	4	12	24	14	3	9	13	36	13
CA13 SWW3 [wt %]	0.29	30.22	1.81	0.44	12.25	19.58	2.21	1.17	0.04	19.46
RSD [%]	28	5	10	22	19	4	8	17	77	16
CA13 SS2 [wt %]	0.30	31.52	1.95	0.50	20.82	17.34	2.84	1.22	0.02	10.46
RSD [%]	21	32	48	43	93	27	29	27	87	60
CA13 DV1 [wt %]	0.44	28.78	1.70	0.58	15.69	19.15	2.19	1.18	0.04	16.90
RSD [%]	35	14	12	29	36	8	16	31	63	46
Average California [wt %]	0.31	27.89	1.65	0.51	14.18	18.19	2.12	1.15	0.04	19.27
RSD [%]	25	19	19	12	27	10	23	13	21	34
IS13 V1 [wt %]	0.25	39.01	1.67	0.74	12.68	20.13	2.53	1.30	0.04	9.67
RSD [%]	18	6	8	25	11	9	7	16	50	32
IS13 V2a [wt %]	0.26	35.97	1.61	0.72	14.02	19.69	2.38	1.58	0.05	9.00
RSD [%]	40	8	10	35	9	4	10	14	55	28
IS13 V3 [wt %]	0.22	32.80	1.34	0.63	10.13	17.40	2.99	1.88	0.04	17.11
RSD [%]	25	9	15	54	18	9	7	21	57	36
Average Israel [wt %]	0.24	35.93	1.54	0.70	12.28	19.08	2.63	1.59	0.04	11.92
RSD [%]	10	9	11	8	16	8	12	18	9	38

elemental abundances. Interestingly, these two groups were collected from two differing sampling areas within California, which are located 120–250 km apart from each other (see Table 1). An explanation might therefore be a slightly different composition of the varnish dust source. Nevertheless, all Californian samples have significantly higher Pb concentrations than the samples from Israel and South Africa (about 10 times more). The explanation therefore might be a larger Pb input by human activity in this area, for example from the previous use of leaded gasoline or from power plants (Nowinski et al., 2010; Dorn et al., 2012b).

By combining EPMA with its 2 μm spatial resolution, and fs LA-ICP-MS, each analyzed varnish coating can be extrapolated back to a manganese free end member, which differs for the various sampling locations. Furthermore, future fs LA-ICP-MS measurements provide the possibility to add compositional variations to areas of a given climate. Adding STXM–NEXAFS at the nm scale, layers in the nm range can also be observed, and C abundances and speciation can be detected and characterized.

4. Conclusions

Rock varnishes show chemical and structural features at the μm to nm scale. The most striking ones are layerings, mineral grain inclusions, and cavities within the varnish. Internal layerings in the 100–500 nm range within the coatings are defined by differing Mn, Fe, and C abundances. Cavities lined by Mn, Fe, and C rich material were found in the underlying rocks of the Californian and Israeli samples, close to and in contact with the varnish coating. The South African samples differ from those from the other analyzed locations at all scales, based on elemental ratios and internal structures without Mn and Fe layering, larger mineral grains, and bigger cavities than the other samples.

The SiO₂ contents of the Mn free end members are independent of the composition of the underlying rock. The SiO₂ concentrations in these Mn free end members are similar to those in dust from different locations, with 50–75% SiO₂ (Moreno et al., 2006; Castillo et al., 2008). The Israeli end member is at the lower end of the range (about 50%) and the Californian and South African end members are in the middle of the range of dust values (about 60%).

The analyzed coatings from different regions can be distinguished by their elemental ratios. The Californian samples can be further separated into two sub-regions that are about 120–250 km apart. Bulk analyses of the coatings show that of the major elements, only Mn and Fe are enriched in comparison to the upper continental crust (Rudnick and Gao, 2003), whereas many trace elements, such as Pb, Co, Ni, Ba, the REEs, U, Th, and Y, are significantly enriched. These enrichments occur in all samples, but differ in their magnitude. Ratio plots of Pb/Ni vs. Mn/Ba show similarities within one sampling location and significant differences between the various regions. The MnO₂/Fe₂O₃ ratios show significant differences (a factor of 10 to 100) between the South African varnish samples and those collected in Israel and California. However, a significant positive Ce anomaly was detected in all samples, which might be an indicator for a direct atmospheric deposition of the REEs, and therefore an atmospheric contribution to the origin of all varnish coatings analyzed. A positive correlation between Ce and Mn was observed for the Israeli and Californian varnish samples, though no correlation was found concerning the South African rock varnish samples.

Carbon was found in every analyzed FIB sample, but in the Israeli sample it was found solely along cracks and fissures. In this sample the carbon could have been introduced subsequent to the varnish genesis, unlike in the other samples, where C was detected as layers or cavity linings. The C signatures, analyzed by STXM–NEXAFS, are dominated by carboxylate functionalities and are therefore indicators of a biological contribution to the varnish composition. Whether these organic contributions triggered the varnish growth, or if the availability of a solid and stable inorganic crust allowed organisms to accrete, or if the organic material was incorporated from particles with an atmospheric origin cannot be determined up to now.

Profile plots of the varnish measurements perpendicular to its growth direction display nicely the transition metal variations within the varnish. Such profiles display internal features, such as layerings within the varnish, and may be used for paleoclimate reconstruction (Dorn, 1984; Liu and Broecker, 2013). The profiles vary within one location and even within one rock, and differ significantly between different sampling countries.

The differences in structure and chemical composition found in our samples suggest at least two different groups of the analyzed varnish,

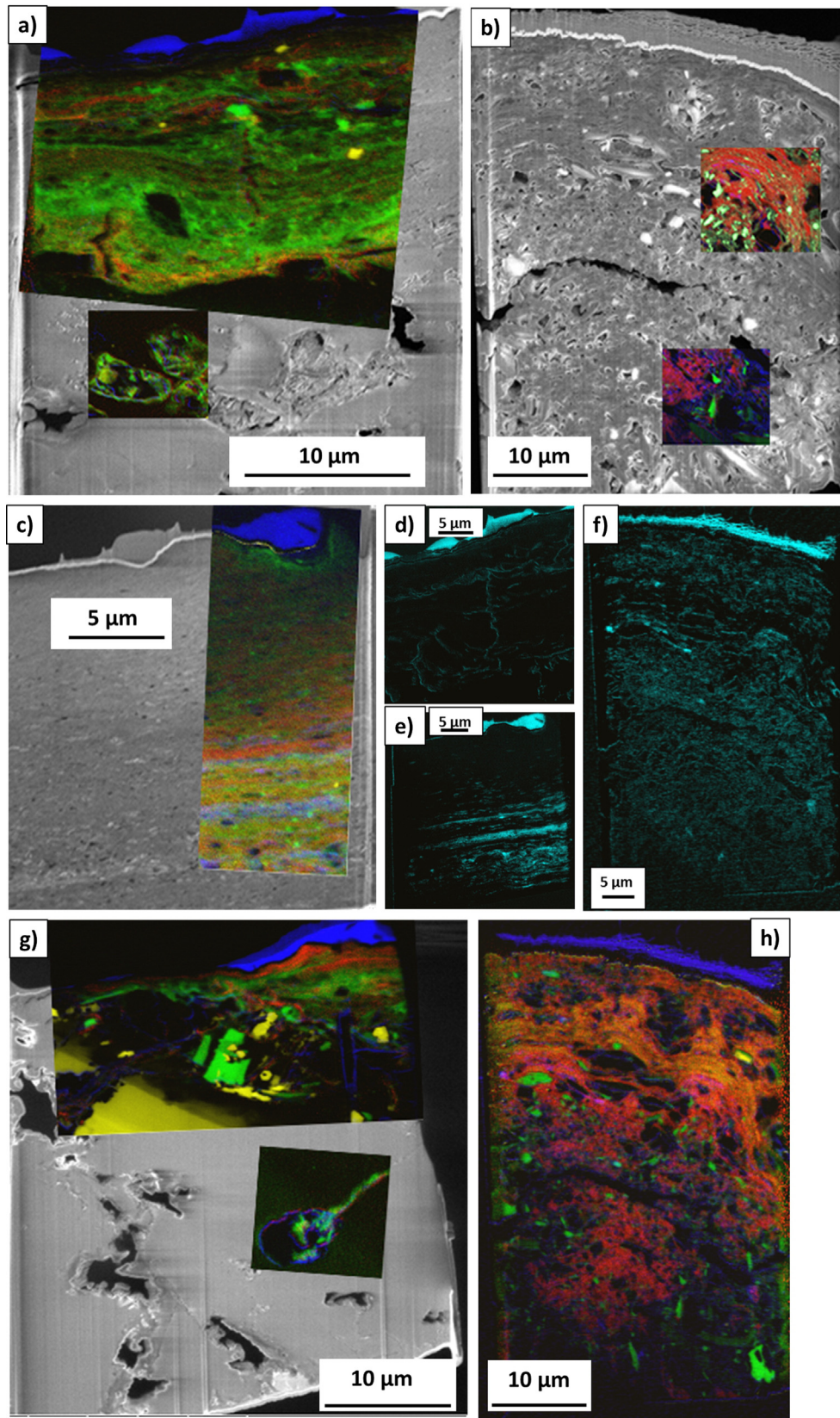


Fig. 10. FIB slices with element maps to display the elemental distribution. Color keys for the multi-element maps: red: Mn; green: Fe; blue: C; yellow: Ca. a) FIB slice of IS13 V1 with mapped varnish area and cavity fillings. b) FIB slice of SA13 mM-f with selected mapped areas. h) Map of the whole FIB-prepared varnish SA13 mM-f. c) FIB slice of CA14 JC-8 with selected mapped area. g) FIB-prepared varnish sample CA14 DV11 with mapped cavity filling and thin varnish. d), e), f) C-maps of the samples, C mapped in blue. d) sample IS13 V1, e) sample CA14 JC-8, f) sample SA13 mM-f. The Pt coating on top of the samples (displayed in the FIB slices as a light colored cover with a gray topping) shows C enrichments that are not related to the varnish but to the metallo-organic Pt precursor.

one represented by the South African samples, the other by the Californian and Israeli samples. One may even distinguish three categories, where the Israeli samples represent a third, carbon-poor category. Further investigations are necessary to see whether the differences observed here can be generalized to other regions, and how they can be used to resolve the enigma of the formation of rock varnishes.

Supplementary data to this article can be found online at <http://dx.doi.org/10.1016/j.chemgeo.2015.06.023>.

Acknowledgments

This work was supported by the Max Planck Graduate Center with the Johannes Gutenberg University Mainz (MPGC), the Max Planck Society, and King Saud University. The ALS is supported by the Director, Office of Science, Office of Basic Energy Sciences, of the US Department of Energy under Contract DE-AC02-05CH11231. We thank the Helmholtz-Zentrum Berlin for the allocation of the synchrotron radiation beamtime at BESSY II. Sampling of desert varnish in Israel was conducted during a granted ExpeER project. We furthermore thank Maik Biegler who prepared the varnish thin and thick sections, Jan-David Förster who helped with the thin section preparation and the STXM measurements, Tanzhuo Liu who provided the sample CA WS-18, and Michael Bechtel (BESSY) who always helps a lot with the STXM sessions.

References

- Armstrong, J.T., 1991. Quantitative elemental analysis of individual microparticles with electron beam instruments. In: Heinrich, K.F.J., Newbury, D.E. (Eds.), *Electron Probe Quantitation*. Plenum Press, pp. 261–315.
- Broecker, W.S., Liu, T., 2001. Rock varnish: record of desert wetness? *GSA Today* 4–10 (August: 4–10).
- Castillo, S., Moreno, T., Querol, X., Alastuey, A., Cuevas, E., Herrmann, L., Mounkaila, M., Gibbons, W., 2008. Trace element variation in size-fractionated African desert dusts. *J. Arid Environ.* 72 (6), 1034–1045.
- Dorn, R.L., 1984. Cause and implications of rock varnish microchemical laminations. *Nature* 310 (5980), 767–770.
- Dorn, R.L., 2008. Rock Varnish in Geochemical Sediments and Landscapes. In: Nash, D.J., McLaren, S.J. (Eds.), *Blackwell Publishing Ltd.*, Oxford, UK, pp. 246–297 (Chapter 8).
- Dorn, R.L., Krinsley, D.H., Ditto, J., 2012a. Revisiting Alexander von Humboldt's initiation of rock coating research. *J. Geol.* 120 (1), 1–14.
- Dorn, R.L., Moore, G., Pagan, E.O., Bostwick, T.W., King, M., Ostapuk, P., 2012b. Assessing early Spanish explorer routes through authentication of rock inscriptions. *Prof. Geogr.* 64 (3), 415–429.
- Dorn, R.L., Krinsley, D.H., Langworthy, K.A., Ditto, J., Thompson, T.J., 2013. The influence of mineral detritus on rock varnish formation. *Aeolian Res.* 10, 61–76.
- Engel, C.G., Sharp, R.P., 1958. Chemical data on desert varnish. *Geol. Soc. Am. Bull.* 69 (5), 487.
- Follath, R., Schmidt, J.S., Weigand, M., Fauth, K., 2010. The X-ray microscopy beamline UE46-PGM2 at BESSY. In: Garrett, R., Gentle, I., Nugent, K., Wilkins, S. (Eds.), *Sri 2009: The 10th International Conference on Synchrotron Radiation Instrumentation*. AIP Conference Proceedings, pp. 323–326.
- Garvie, L.A.J., Burt, D.M., Buseck, P.R., 2008. Nanometer-scale complexity, growth, and diagenesis in desert varnish. *Geology* 36 (3), 215–218.
- Goldsmith, Y., Stein, M., Enzel, Y., 2014. From dust to varnish: geochemical constraints on rock varnish formation in the Negev Desert, Israel. *Geochim. Cosmochim. Acta* 126, 97–111.
- Hodge, V.F., Farmer, D.E., Diaz, T., Orndorff, R.L., 2005. Prompt detection of alpha particles from Po-210: another clue to the origin of rock varnish? *J. Environ. Radioact.* 78 (3), 331–342.
- Jochum, K.P., Stoll, B., Herwig, K., Willbold, M., 2007. Validation of LA-ICP-MS trace element analysis of geological glasses using a new solid-state 193 nm Nd:YAG laser and matrix-matched calibration. *J. Anal. At. Spectrom.* 22 (2), 112–121.
- Jochum, K.P., Stoll, B., Weis, U., Jacob, D.E., Mertz-Kraus, R., Andreae, M.O., 2014. Non-matrix-matched calibration for the multi-element analysis of geological and environmental samples using 200 nm femtosecond LA-ICP-MS: a comparison with nanosecond lasers. *Geostand. Geoanal. Res.* 38 (3), 265–292.
- Kilcoyne, A.L.D., Tylliszczak, T., Steele, W.F., Fakra, S., Hitchcock, P., Franck, K., Anderson, E., Harteneck, B., Rightor, E.G., Mitchell, G.E., Hitchcock, A.P., Yang, L., Warwick, T., Ade, H., 2003. Interferometer-controlled scanning transmission X-ray microscopes at the Advanced Light Source. *J. Synchrotron Radiat.* 10, 125–136.
- Krinsley, D., Dorn, R.L., DiGregorio, B., 2009. Astrobiological implications of rock varnish in Tibet. *Astrobiology* 9 (6), 551–562.
- Krinsley, D.H., Dorn, R.L., DiGregorio, B.E., Langworthy, K.A., Ditto, J., 2012. Rock varnish in New York: an accelerated snapshot of accretionary processes. *Geomorphology* 138 (1), 339–351.
- Krinsley, D., Ditto, J., Langworthy, K., Dorn, R.L., Thompson, T., 2013. Varnish microlaminations: new insights from focused ion beam preparation. *Phys. Geogr.* 34 (3), 159–173.
- Liu, T.H., Broecker, W.S., 2000. How fast does rock varnish grow? *Geology* 28 (2), 183–186.
- Liu, T., Broecker, W.S., 2013. Millennial-scale varnish microlamination dating of late Pleistocene geomorphic features in the drylands of western USA. *Geomorphology* 187, 38–60.
- Liu, T.Z., Dorn, R.L., 1996. Understanding the spatial variability of environmental change in drylands with rock varnish microlaminations. *Ann. Assoc. Am. Geogr.* 86 (2), 187–212.
- Macholdt, D.S., Jochum, K.P., Stoll, B., Weis, U., Andreae, M.O., 2014. A new technique to determine element amounts down to femtograms in dust using femtosecond laser ablation-inductively coupled plasma-mass spectrometry. *Chem. Geol.* 383, 123–131.
- Moreno, T., Querol, X., Castillo, S., Alastuey, A., Cuevas, E., Herrmann, L., Mounkaila, M., Elvira, J., Gibbons, W., 2006. Geochemical variations in aeolian mineral particles from the Sahara-Sahel Dust Corridor. *Chemosphere* 65 (2), 261–270.
- Northup, D.E., Snider, J.R., Spilde, M.N., Porter, M.L., van de Kamp, J.L., Boston, P.J., Nyberg, A.M., Bargar, J.R., 2010. Diversity of rock varnish bacterial communities from Black Canyon, New Mexico. *J. Geophys. Res. Biogeosci.* 115.
- Nowinski, P., Hodge, V.F., Lindley, K., Cizdziel, J.V., 2010. Elemental analysis of desert varnish samples in the vicinity of coal-fired power plants and the Nevada test site using laser ablation ICP-MS. *Chem. Biomed. Methods J.* 3, 153–168.
- Nowinski, P., Hodge, V.F., Gerstenberger, S., Cizdziel, J.V., 2013. Analysis of mercury in rock varnish samples in areas impacted by coal-fired power plants. *Environ. Pollut.* 179, 132–137.
- Ohta, A., Kawabe, I., 2001. REE(III) adsorption onto Mn dioxide (δ -MnO₂) and Fe oxyhydroxide: Ce(III) oxidation by δ -MnO₂. *Geochim. Cosmochim. Acta* 65 (5), 695–703.
- Perry, R.S., Adams, J.B., 1978. Desert varnish: evidence for cyclic deposition of manganese. *Nature* 276 (5687), 489–491.
- Perry, R.S., Kolb, V.M., 2004. Biological and organic constituents of desert varnish: review and new hypotheses. In: Hoover, R.B., Rozanov, A.Y. (Eds.), *Instruments, Methods, and Missions for Astrobiology VII* 5163, pp. 202–217.
- Perry, R.S., Lynne, B.Y., Sephton, M.A., Kolb, V.M., Perry, C.C., Staley, J.T., 2006. Baking black opal in the desert sun: the importance of silica in desert varnish. *Geology* 34 (7), 537–540.
- Post, J.E., 1999. Manganese oxide minerals: crystal structures and economic and environmental significance. *Proc. Natl. Acad. Sci. U. S. A.* 96 (7), 3447–3454.
- Potter, R.M., Rossman, G.R., 1979. The manganese- and iron-oxide mineralogy of desert varnish. *Chem. Geol.* 25, 79–94.
- Reneau, S.L., Raymond, R., Harrington, C.D., 1992. Elemental relationships in rock varnish stratigraphic layers, Cima volcanic field, California – implications for varnish development and the interpretation of varnish chemistry. *Am. J. Sci.* 292 (9), 684–723.
- Rudnick, R.L., Gao, S., 2003. 3.01 – Composition of the Continental Crust 3. *Treatise On Geochemistry*, Elsevier Ltd., pp. 1–64.
- Spilde, M.N., Melim, L.A., Northup, D.E., Boston, P.J., 2013. Anthropogenic lead as a tracer of rock varnish growth: implications for rates of formation. *Geology* 41 (2), 263–266.
- Thiagarajan, N., Lee, C.T.A., 2004. Trace-element evidence for the origin of desert varnish by direct aqueous atmospheric deposition. *Earth Planet. Sci. Lett.* 224 (1–2), 131–141.
- Von Humboldt, A., Bonpland, A., 1819. *Voyage aux régions équinoxiales du nouveau continent*. pp. 299–304 (II(Book VII Chapter XX)).
- Wang, X., Zeng, L., Wiens, M., Schlossmacher, U., Jochum, K.P., Schroeder, H.C., Mueller, W.E.G., 2011. Evidence for a biogenic, microorganismal origin of rock varnish from the Gangdese Belt of Tibet. *Micron* 42 (5), 401–411.
- Wayne, D.M., Diaz, T.A., Fairhurst, R.J., Orndorff, R.L., Pete, D.V., 2006. Direct major- and trace-element analyses of rock varnish by high resolution laser ablation inductively-coupled plasma mass spectrometry (LA-ICPMS). *Appl. Geochem.* 21 (8), 1410–1431.